

Thin-sheet modelling of lithospheric deformation and surface mass transport

Ivone Jiménez-Munt^{a,*}, Daniel Garcia-Castellanos^{b,*}, Manel Fernandez^c

^a Department of Earth Sciences, University College London, London, United Kingdom

^b Dept. Tectonics, Faculty of Earth and Life Sciences, Vrije Universiteit, Amsterdam, The Netherlands

^c Inst. of Earth Sciences 'Jaume Almera' (CSIC), Barcelona, Spain

Received 4 August 2004; received in revised form 1 June 2005; accepted 5 August 2005

Abstract

We study the effects of incorporating surface mass transport and the gravitational potential energy of both crust and lithospheric mantle to the viscous thin sheet approach. Recent 2D (cross-section) numerical models show that surface erosion and sediment transport can play a major role in shaping the large-scale deformation of the crust. In order to study these effects in 3D (planform view), we develop a numerical model in which both the dynamics of lithospheric deformation and surface processes are fully coupled. Deformation is calculated as a thin viscous layer with a vertically-averaged rheology and subjected to plane stresses. The coupled system of equations for momentum and energy conservation is solved numerically. This model accounts for the isostatic and potential-energy effects due to crustal and lithospheric thickness variations. The results show that the variations of gravitational potential energy due to the lateral changes of the lithosphere–asthenosphere boundary can modify the mode of deformation of the lithosphere. Surface processes, incorporated to the model via a diffusive transport equation, rather than just passively reacting to changes in topography, play an active role in controlling the lateral variations of the effective viscosity and hence of the deformation of the lithosphere.

© 2005 Elsevier B.V. All rights reserved.

Keywords: Gravitational potential energy; Geodynamics; Strain rate; Erosion; Sedimentation; Lithosphere–asthenosphere boundary

1. Introduction

The thin-sheet approach has been widely used to study the large scale deformation of the lithosphere when it is submitted to external forces. This approach considers the lithosphere as a thin viscous layer (Vilotte et al., 1982) or as two layers, mantle and crust (Bird, 1989) with vertically-averaged rheology and subjected to plane stresses. Early thin-sheet models accounted for mechanical deformation only (Eng-

land and McKenzie, 1983), whereas later versions incorporated temperature-dependent viscosity (Bird, 1989; Sonder and England, 1989). Lateral variations of lithospheric stiffness together with specific boundary conditions (indentation, convergence velocity, etc) have been incorporated to thin-sheet models to explain the deformation observed in collisional settings, such as the India–Asia convergence zone (e.g., England and Houseman, 1985; Vilotte et al., 1986; Neil and Houseman, 1997; and reference therein), western North America (Bird, 1988), north-eastern Brazil (Tommasi et al., 1995), the Iranian plateau (Sobouti and Arkani-Hamed, 1996), central-western Europe (Marotta et al., 2001), Paleozoic deformation of Aus-

* Corresponding authors. Inst. of Earth Sciences 'Jaume Almera' (CSIC), Lluís Solé i Sabarís s/n, 08028 Barcelona, Spain.

E-mail address: ivone@ija.csic.es (I. Jiménez-Munt).

tralia (Braun and Shaw, 2001), or the crustal deformation driven by basal velocity (Ellis et al., 1995). Despite the success of these models in reproducing the main trends of orogenic topography and crustal thickness, several oversimplifications limit the capability of reproducing some tectonic evolution where the depth (lithosphere–asthenosphere boundary) and/or surface processes play an important role. Stiff and weak zones are often incorporated in to some of these models as lateral variations of a parameter B , which includes the dependence of the vertically averaged viscosity of the lithosphere on temperature and composition, and it is therefore indistinctly attributed to changes in the rock rheology, thermal properties, or lithosphere thicknesses. In these works they used the dimensionless Argand number as a measure of the magnitude of buoyancy forces caused by gradients in crustal thickness relative to the viscous stresses. Values of the Argand number derived from lithospheric-scale modelling range between 0 (very strong) and 50 (very soft), but unfortunately these values are not always consistent with experimentally determined rheological rock properties, and the Argand number remains an arbitrary parameter of thin-sheet models (England and Houseman, 1989). In spite of the strong temperature dependence of viscosity (Sonder and England, 1986; Neil and Houseman, 1997), most thin-sheet numerical experiments on collisional settings do not include thermal calculations. Several authors have discussed the occurrence of stiff/weak areas in terms of lateral variations of the thermal regime (e.g., Molnar and Tapponnier, 1981; England and Houseman, 1985; Tommasi et al., 1995; Neil and Houseman, 1997) but the lack of a full thermo-mechanical formulation has impeded studying the feedback effects between deformation and temperature changes.

One of the most influential rock properties on temperature distribution at lithospheric scale is the heat production associated with natural radioactive decay, which amounts about 40% of the total heat released to the atmosphere by the continental lithosphere (Pollack and Chapman, 1977). Volumetric heat production measurements range between 0–0.02 $\mu\text{W m}^{-3}$ for mantle rocks, 0.1–1 $\mu\text{W m}^{-3}$ for lower crustal rocks, and 1–4 $\mu\text{W m}^{-3}$ for upper crustal rocks (Wollenberg and Smith, 1987), although depth variations of radiogenic heat production in continental crust have been largely debated in the literature (e.g., Morgan et al., 1987). In previous thin-sheet models, heat production has been either neglected (Sonder and England, 1989) or incorporated as a constant value

for the crust and lithospheric mantle (Bird, 1988, 1989).

Apart from tectonic boundary forces and rheology, thin viscous sheet deformation is also controlled by lateral variations of gravitational potential energy within the plate. Most thin-sheet models calculate these as a function of the crustal thickness variations, assuming constant densities for crust and mantle and neglecting the density contrast between lithosphere and asthenosphere. However, the lithospheric mantle is known to play a significant isostatic role (e.g., Torne et al., 2000; García-Castellanos et al., 2002; Jiménez-Munt et al., 2003). Therefore, calculating gravitational potential energy contrasts and thin-sheet deformation requires a thermo-mechanical model also accounting for the density variations in the lithospheric mantle and the asthenosphere.

Another process that has been systematically overlooked in previous thin-sheet models is surface transport. Although Braun and Shaw (2001) designed a model in which thin-sheet deformation and surface diffusive transport were simultaneously calculated to reproduce the Australian Palaeozoic lithospheric deformation, a detailed study of how these two processes interact is still needed. It has long been understood that tectonic uplift controls the atmosphere and ocean circulations and therefore also the global climate, which in turn affects the localisation of rock weathering and erosion (Ruddiman, 1997; and references therein). Inversely, over the last fifteen years it has become clear that both erosion and climate can also have a significant impact on the tectonic evolution of orogens. This has resulted in a number of papers using both analogue and numerical modeling techniques to study the interplay between surface and crustal-scale processes. Numerical models have demonstrated that syntectonic erosion affects the localisation of deformation within the orogenic wedge and have constrained the conditions under which these feedback mechanisms lead to steady state topography (Jamieson and Beaumont, 1988, 1989; Beaumont et al., 1992, 2000; Willet, 1999; Willett and Brandon, 2002). Surface mass redistribution produces noticeable pressure changes at deep crustal levels, hence influencing on the timing of fault activation and the tectonic evolution of orogens. Surface transport has also been proposed to prevent collapse of an intracontinental range as removal of material from topographic heights and deposition in the foreland oppose to spreading of the crustal root (Avouac and Burov, 1996). In addition to the effects of erosion, the load of sediment in foreland basins formed in front of orogens induces forward propagation of thrusting (Cob-

bold et al., 1993; Mugnier et al., 1997; Persson and Sokoutis, 2002; Persson et al., 2004).

Finally, most of these studies are limited to a 2D cross-section approach, whereas orogen-basin systems often present a marked three-dimensionality that influences both tectonics and, particularly, surface transport.

In this work, we apply a finite difference numerical code called *Uhuru*, based on a program initially designed for the neotectonic study of the Africa–Eurasia plate boundary from Azores to Gibraltar (Jiménez-Munt et al., 2001). The present model is able to deform the crustal and mantle boundaries, allowing for large amounts of deformation and tracking the long-term temperature evolution, overcoming the limitations described above. Relative to previous thin-sheet models,

the main innovative aspects of this code are: 1) coupled calculation of the thermal and mechanical equations governing lithospheric compressional deformation under the thin viscous sheet approach; 2) isostatic and potential-energy effects of lithospheric thickness variations; 3) exponential decrease with depth of radiogenic heat production within the crust; 4) erosion and sedimentation are calculated coupled with the lithospheric processes. This tool allows us to evaluate the 3D interaction between lithospheric deformation, thermal evolution, and surface processes during continental collision (Fig. 1a).

In order to study this interaction, we choose a scenario where erosion/sediment accumulation and lateral variations of the base of the lithosphere are large. Thus,

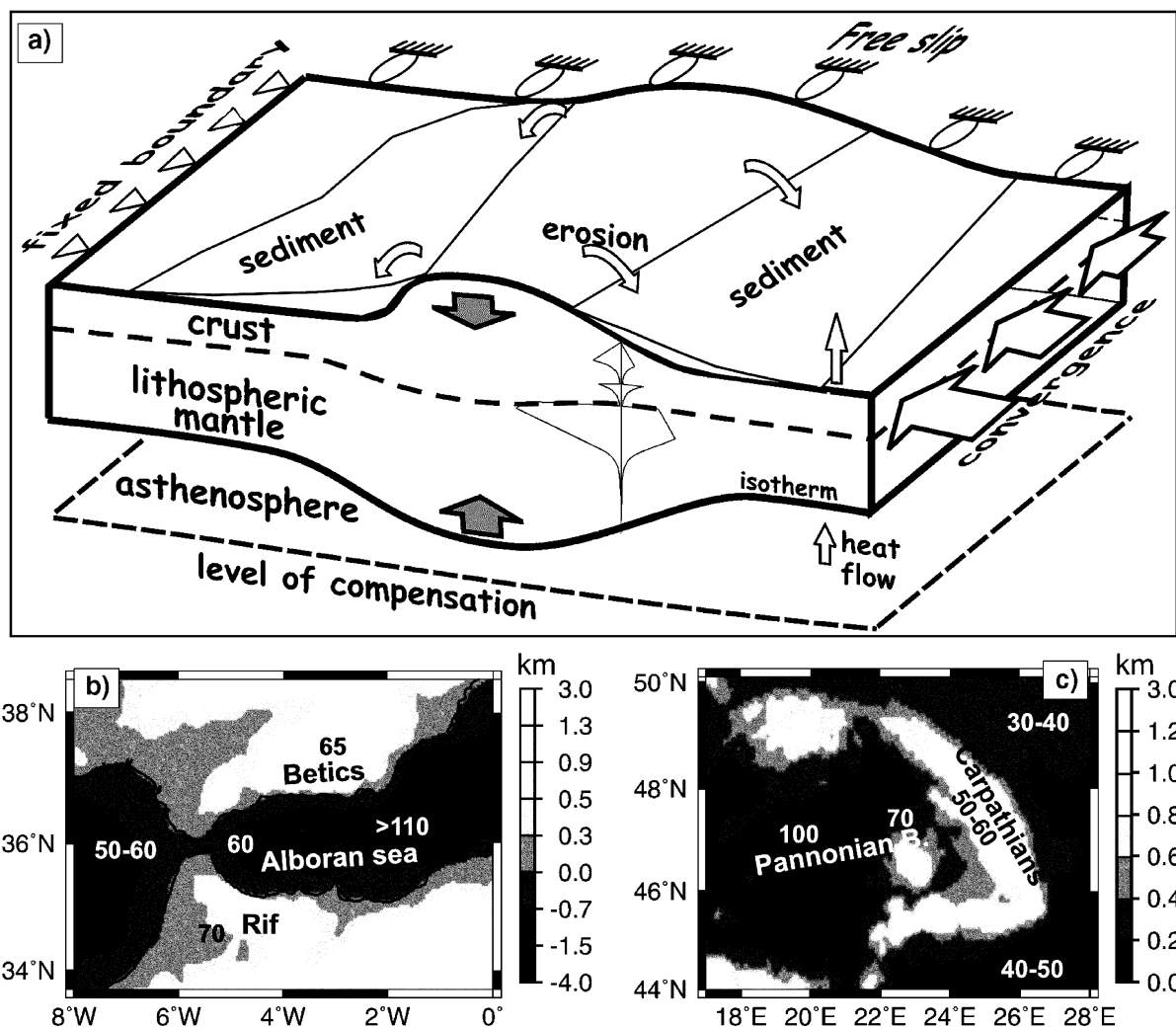


Fig. 1. a) Conceptual cartoon of the numerical model, integrating lithospheric-scale deformation and surface transport. b) and c) show the topography (grey shading), and mean surface heat flow values (bold numbers, mW/m²) of the Betic–Alboran and the Carpathian–Pannonian regions, on which the synthetic models of this study are inspired.

we have chosen as initial set-up an elevated arc of thickened crust and lithosphere, surrounding a basin with shallow lithosphere–asthenosphere boundary. This scenario is inspired on continental back-arc settings as the Betic–Rif–Alboran and the Carpathian–Pannonian systems (Fig. 1b,c).

2. Fundamentals of thin-sheet deformation

The thin-sheet approach for lithospheric deformation assumes local isostasy and vertical integration of the lithospheric strength to reduce the three-dimensional problem to a planform model, where the horizontal velocity components do not change on depth (England and McKenzie, 1983; Bird, 1989). The geodynamic finite-difference code calculates the lithospheric deformation and stress distribution by coupling the equilibrium and constitutive equations for a highly viscous fluid and considering the gravitational potential energy related to crustal and lithospheric mantle thickness variations (Jiménez-Munt et al., 2001).

The equilibrium equation for the lithosphere is given by,

$$\frac{\partial \sigma_{ij}}{\partial x_j} + \rho g_i = 0 \quad i, j = 1, 2, 3 \quad (1)$$

where $\vec{g} = (0, 0, g)$ is the acceleration due to gravity and $\sigma_{ij} = \tau_{ij} + 1/3 \delta_{ij} \sigma_{kk}$ is the total stress; σ_{kk} is the sum of the terms of the diagonal from the stress tensor, $\sigma_{kk} = \sigma_{11} + \sigma_{22} + \sigma_{33}$, and $\delta_{ij} = 1$ if $i = j$ and $\delta_{ij} = 0$ if $i \neq j$, where index 3 corresponds to the vertical component. The deviatoric stress, τ_{ij} , is related to the strain rate through the constitutive equation (Sonder and England, 1989; Ellis et al., 1995),

$$\tau_{ij} = 2\eta \dot{\epsilon}_{ij} \quad i, j = 1, 2, 3 \quad (2)$$

where η is the effective viscosity and $\dot{\epsilon}_{ij}$ is the strain rate tensor.

Under the assumption of plane stress, where the vertical shear stress are negligible ($\dot{\epsilon}_{13} = \dot{\epsilon}_{31} = \dot{\epsilon}_{23} = \dot{\epsilon}_{32} = 0$), the vertical component of the stress σ_{33} yields,

$$\frac{\partial \sigma_{33}}{\partial x_3} = -\rho g. \quad (3)$$

These assumptions allow the deformation of the lithosphere to be treated in terms of vertically-averaged magnitudes. Therefore, the momentum equations are vertically averaged along depth x_3 within the plate. Considering Eq. (3), the fluid incompressibility $\dot{\epsilon}_{33} = -(\dot{\epsilon}_{11} + \dot{\epsilon}_{22})$ and the relation between the strain

rate and the velocity field $\dot{\epsilon}_{ij} = \frac{1}{2} \left(\frac{\partial u_i}{\partial x_j} + \frac{\partial u_j}{\partial x_i} \right)$, the horizontal components of Eq. (1) result in

$$\begin{aligned} \frac{\partial}{\partial x_1} \left[2\eta \left(2 \frac{\partial u_1}{\partial x_1} + \frac{\partial u_2}{\partial x_2} \right) \right] + \frac{\partial}{\partial x_2} \left[\eta \left(\frac{\partial u_1}{\partial x_2} + \frac{\partial u_2}{\partial x_1} \right) \right] \\ = \frac{\partial \bar{p}}{\partial x_1} \end{aligned}$$

$$\begin{aligned} \frac{\partial}{\partial x_1} \left[\eta \left(\frac{\partial u_2}{\partial x_1} + \frac{\partial u_1}{\partial x_2} \right) \right] + \frac{\partial}{\partial x_2} \left[2\eta \left(\frac{\partial u_1}{\partial x_1} + 2 \frac{\partial u_2}{\partial x_2} \right) \right] \\ = \frac{\partial \bar{p}}{\partial x_2} \end{aligned}$$

or, written more compactly,

$$\begin{aligned} \frac{\partial}{\partial x_j} \left[\eta \left(\frac{\partial u_i}{\partial x_j} + \frac{\partial u_j}{\partial x_i} \right) \right] + \frac{\partial}{\partial x_i} \left[2\eta \left(\frac{\partial u_1}{\partial x_1} + \frac{\partial u_2}{\partial x_2} \right) \right] \\ = \frac{\partial \bar{p}}{\partial x_i} \quad (4) \end{aligned}$$

where $i, j = 1, 2$ are the horizontal components; u_1 and u_2 are horizontal components of the velocity vector and they are the two unknowns; and \bar{p} is the depth-averaged vertical stress over the plate to include the gravitational potential energy variations induced by lateral variations in crustal and lithospheric mantle thicknesses, therefore, this value also depends on the asthenosphere density.

The vertical strain rate is calculated assuming incompressibility, leading to the following expression for the changes in crustal thickness in an Eulerian reference system,

$$\frac{\partial s}{\partial t} + \vec{\nabla} s \cdot \vec{u} = \dot{\epsilon}_{33} s \quad (5)$$

where s is the crustal thickness, t is time and \vec{u} is the velocity vector.

The effective viscosity η depends on temperature and velocity, and it is calculated from the depth-integral of the yield stress envelope. Deformation occurs by frictional sliding or dislocation creep. At each depth, the yield stress is given by the lesser of the brittle and ductile strength (Jiménez-Munt et al., 2001). The frictional sliding is a function of depth x_3 , according to $\tau_{\text{brittle}} = \beta x_3$, where the brittle failure coefficient β is the yield stress gradient depending on the type of fault, the angle of fracture and on the pore-pressure. Following Lynch and Morgan (1987), this coefficient amounts 16 MPa/km for extension and 40 MPa/km for compression. Ductile deformation is governed by the power law creep equation when the applied stresses are less than 200 MPa and by the Dorn law equation for larger

stresses (e.g., Goetze and Evans, 1979). Then, the ductile deformation is given by,

$$\text{Power law : } \tau_{\text{ductile}} = \left(\frac{\dot{\epsilon}}{A} \right)^{1/n} \exp \left(\frac{Q}{nRT} \right)$$

$\tau \leq 200$ MPA

$$\text{Dorn law : } \tau_{\text{ductile}} = \sigma_d \left[1 - \left(\frac{RT}{Q_d} \ln \left(\frac{\dot{\epsilon}_d}{\dot{\epsilon}} \right) \right)^{1/2} \right]$$

$\tau > 200$ MPA (6)

where A , Q , n , σ_d , Q_d and $\dot{\epsilon}_d$ are material constants depending on the rock-type, R is the gas constant and T is the absolute temperature. $\dot{\epsilon}$ is an effective strain rate given by the second invariant of the strain rate tensor

$$\dot{\epsilon} = \left(\frac{1}{2} (\dot{\epsilon}_{11}^2 + \dot{\epsilon}_{22}^2 + \dot{\epsilon}_{33}^2) + \dot{\epsilon}_{12}^2 \right)^{1/2}.$$

The experimental determinations of the rheological parameters show large uncertainties, and different data sets have been used in literature to describe the mechanical behaviour of rocks leading to different strength envelopes (e.g., Fernández and Ranalli, 1997). We have considered that the crust is divided into a 2/3 thick upper crust with a quartz-rich composition and a 1/3 thick lower crust with an intermediate composition between diabase and diorite. In this work we have used a representative rheological parameters (Table 1) obtained from average values from different studies (Lynch and Morgan, 1987). The effective viscosity η is calculated from the depth integral of the yield stress envelope and it is a function of the temperature and the local strain rate.

Eq. (4) expresses that, for given boundary conditions (stress or velocities), the velocity field on the thin plate

depends on the lateral variations of the viscosity and gravitational potential energy. The effective viscosity depends on the plate strength and therefore, on the rheology of the lithosphere. A hard lithosphere can hold higher variations of the gravitational potential energy related to crustal and/or lithospheric mantle thickness variations. In contrast, a soft lithosphere doesn't permit large gradients of vertical stresses, preventing large lateral thickness variations. On other hand, the gravitational potential energy is a function of the density and thickness of sediments, crust, lithospheric mantle and asthenosphere, and doesn't depend on the rheology.

Moreover, the integrated strength profile of the lithosphere determined by the rheological constitutive relation of the dominant minerals is strongly temperature dependent. The temperature distribution is given by,

$$\frac{dT}{dt} = \frac{\kappa}{K} \vec{\nabla} \cdot \left(K \cdot \vec{\nabla} T \right) + \frac{\kappa}{K} H \quad (7)$$

where κ is the thermal diffusivity, K is the thermal conductivity, H is the volumetric radiogenic heat production (decreasing exponentially with depth in the crust and sediments, $H(z) = H_{\text{surf}} \exp(-x_3/b)$, and constant in the lithospheric mantle; Table 1), and $\frac{dT}{dt} = \frac{\partial T}{\partial t} + \vec{u} \cdot \vec{\nabla} T$ is the total derivative and therefore includes the advective term. The thermal model is simplified by considering only the vertical component of heat conduction. Eq. (7) is solved in 1-D using the finite difference technique and fixing the temperature at surface and at 300 km depth in the asthenosphere (Table 1). The lithosphere–asthenosphere boundary is defined as the depth to a reference isotherm (in this work $T_{\text{lit}} = 1600$ K), which is affected by thermal advection (deformation), thermal conduction, and radiogenic heat production. To simulate the adiabatic

Table 1

Densities: water, sediments, crust and asthenosphere (ρ_w , ρ_{sed} , ρ_c , ρ_a)	1030, 2450, 2800, 3200 kg/m ³
lithospheric mantle: $\rho_m = \rho_a (1 + (T_{\text{lit}} - T_{\text{moho}}) \alpha / 2)$	
Volumetric thermal expansion of lithospheric mantle (α)	$3.5 \cdot 10^{-5} \text{ K}^{-1}$
Base of the lithosphere, isotherm (T_{lit})	1600 K
Conductivities: sediments, crust, lithospheric mantle, asthenosphere	2.4, 3, 3.2, 100 W m ⁻¹ K ⁻¹
Heat production: sediments+crust, lithospheric mantle (x_3 : depth, km)	$2.5 \cdot \exp(-x_3/15)$, 0 $\mu\text{W m}^{-3}$
Surface, bottom ($x_3=300$ km) temperature. Boundary condition Eq. (7)	273, 1800 K
Thermal diffusivity	$1 \cdot 10^{-6} \text{ m}^2/\text{s}$
Rheological	Upper crust: A [MPa ⁻ⁿ s ⁻¹], n , Q [kJ mol ⁻¹] Lower crust: A [MPa ⁻ⁿ s ⁻¹], n , Q [kJ mol ⁻¹] Lithospheric mantle: A [MPa ⁻ⁿ s ⁻¹], n , Q [kJ mol ⁻¹] Dorn law: σ_d [Pa], Q_d [kJ mol ⁻¹], $\dot{\epsilon}_d$ [s ⁻¹]
Reference strain rate	$2.5 \cdot 10^{-8}$, 3, 138 $3.2 \cdot 10^{-3}$, 3, 251 10 ³ , 3, 523 $8.5 \cdot 10^9$, 100, $5.7 \cdot 10^{11}$ $4 \cdot 10^{-16} \text{ s}^{-1}$
Model domain	1500 × 1500 km
Spatial discretization grid (dx_1 , dx_2 , dx_3)	16666, 16666, 340 m
Time step	0.2 My

gradient on the asthenosphere, we have assumed that it has a high thermal conductivity ($\sim 100 \text{ W m}^{-1} \text{ K}^{-1}$). The change in thermal conductivity between lithospheric mantle and asthenosphere is also a dynamic boundary, which moves with the isotherm that defines the base of the lithosphere (T_{lit}) and occurs 20 km beneath this isotherm.

To solve the equilibrium and thermal equations (Eqs. (4) and (7)) we have used the finite difference technique with an Eulerian scheme (the grid is fixed in time). At each time-step and each point of the planform grid we obtain the horizontal velocities from Eq. (4), and the vertical strain rate from the incompressibility condition. From Eq. (5) we calculate the new crustal thickness. Then, we solve vertically the thermal Eq. (7) using the finite difference technique and Crank Nicholson scheme, fixing the temperature at the surface and bottom (Table 1). With this new temperature field, we determine the depth of the base of the lithosphere (fixed isotherm) and the new strength envelope and viscosity.

The power-law rheology implies that the effective viscosity is a function of strain rate; therefore, usually iterative solvers are used to calculate the horizontal components of velocity on Eq. (4). However, we have explored that if the time step is small and velocity changes in time are not abrupt, it is enough to use the previous strain rate to calculate the viscosity at each time step.

The potential of this method is to study in plain view lithospheric deformation processes through time in compressive and/or extensive tectonic settings. Main constraints are elevation, crustal and lithospheric evolution, velocity field, stress direction, tectonic regime, finite rotations and vertical movements.

In the following sections we show the results of several numerical experiments in compressional settings to quantify and evaluate the influence of body forces induced by variations of the topography of the lithosphere–asthenosphere boundary and surface mass-transport processes causing erosion and sedimentation.

3. Reference model (Model 1)

To perform our calculations, we use an initial setting that resembles a planform-curved orogen located next to a backarc basin. Examples for this scenario include (Fig. 1) the orogen-basin systems of Betic–Rif–Alboran (Torne et al., 2000) and Carpathian–Pannonian Basin (Cloetingh et al., 2004). Erosion of more than 5 km of rock from the Middle Miocene to present in the Eastern Carpathians, and sediment accumulations of up to 8 km

in both the Pannonian Basin and the Alborán Basin show that surface mass transport has played a significant role in defining the present crustal thickness distribution. In both cases, the arched planform geometry and the back-arc extension in the core of and orogen seem to be related either to slab retreat or mantle delamination (eastwards in the Carpathians and arguably westwards in the Gibraltar Arc). However, this problematic is beyond the interests of the present study, which is focused on the thermomechanical response to compression once the central basin is already formed.

On Fig. 2, we show the initial geometry adopted for Model 1, which we will use as a reference model hereafter. It consists of an orocline of thickened lithosphere surrounding a thinned-lithosphere basin area. Crustal thickness changes from 17 km in the central basin to 46 km in the orogen and 32 km in the foreland. Initial lithosphere thickness is defined varying between 71 km in the basin to 136 km in the orogen and 120 km in the foreland. Under these conditions and assuming local isostasy and steady-state thermal regime (e.g., Jiménez-Munt et al., 2001), the resulting initial elevation varies from -1.78 km (below sea level) in the basin to 2.15 km in the thickened area and 255 m in the foreland. The thermal and rheological parameters used for this model are shown on Table 1, resulting in the yield stress envelopes displayed in Fig. 2a. These strength envelopes show minimum lithospheric strength in the basin and maximum strength in the foreland. Note that we used representative compositions for the upper and lower crust and the lithospheric mantle; however, other compositions could result in different lateral variations of the lithospheric strength and, therefore, varying the mode of lithosphere deformation. However, it would not affect the conclusions of this study.

Tectonic convergence is implemented as an inflow velocity in the southern and northern boundary (Fig. 2b).

We have performed several models varying the convergence rate from null to 20 mm/yr, in order to see the role of the gravitational potential energy in front of the tectonic compression. Fig. 3 shows the initial velocity field and the vertical strain rate resulting from solving Eq. (4) for the described initial lithospheric geometry and boundary conditions, with a total of 10 mm/yr of convergence rate (5 mm/yr on the northern boundary and 5 mm/yr in the southern boundary; Fig. 3a), and without convergence (Fig. 3b).

The resulting collapse of the mountain chain is not only depending on the rheology of the lithosphere, but

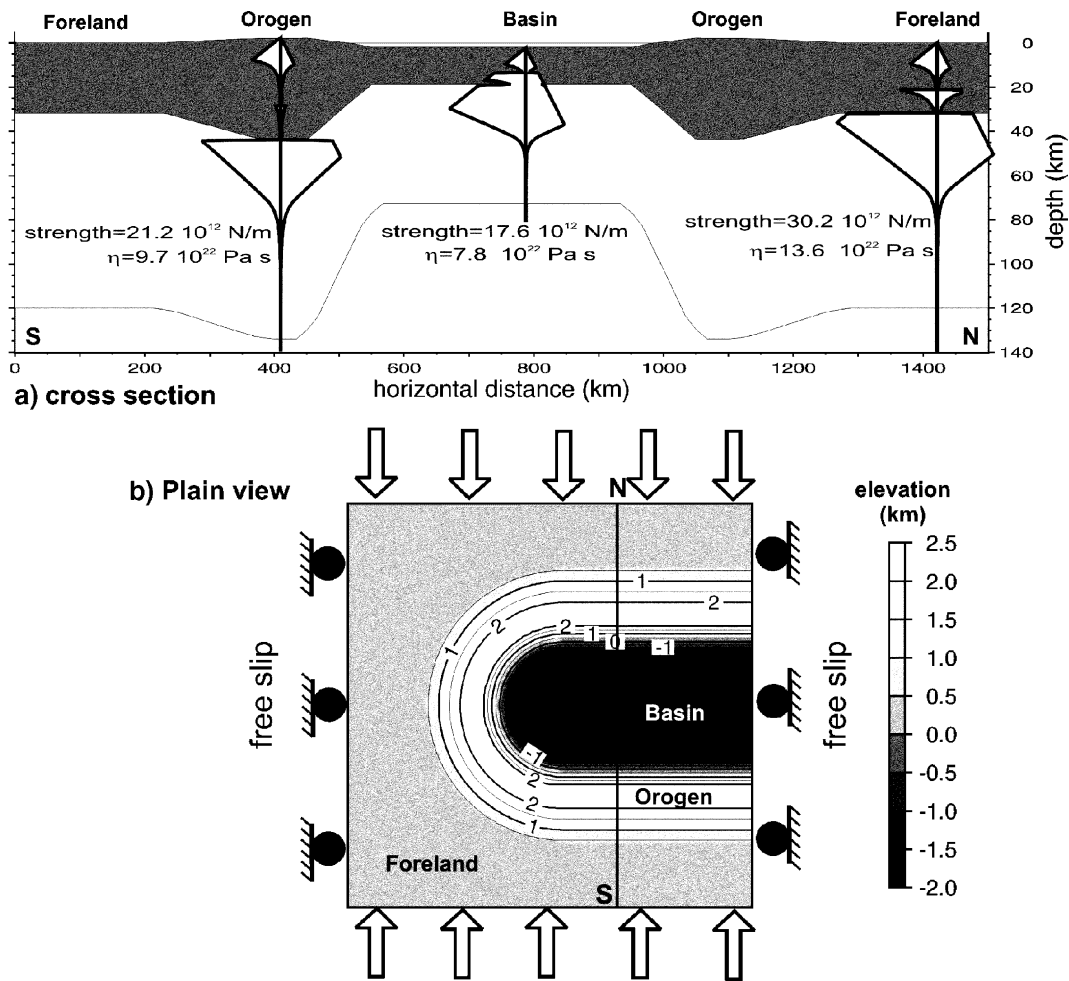


Fig. 2. Initial set up of the reference model. a) Cross-section along the path S–N indicated in b), and stress envelopes at three selected locations. Numbers indicate total (vertically integrated) lithospheric strength (in N/m) and associated viscosity (Pa.s). The parameters used are those from Table 1. b) Plan view of the initial elevation and boundary conditions: convergence velocity to the south and north boundaries, and free slip on the east and west boundaries. Model domain: 1500 × 1500 km.

also is a function of the convergence velocity. For low convergence velocities, the vertical thinning rate due to the gravitational spreading of the orogen can exceed the thickening rate related to convergence and net collapse occurs (Fig. 3b). As seen in Fig. 3, the maximum thickening rates occur initially at the central basin. This is the result of accommodation of shortening in the weaker basin area (Fig. 2a) and the inflow of material towards the basin due to gravitational spreading of the orogen (Fig. 3b). The addition of these two effects explains the rotation towards the east of flow velocity in the western side of the domain (Fig. 3a).

After 25 Myr of 10 mm/yr of convergence rate, both lithosphere and crust have been thickened all over the model domain (Fig. 4). Crustal thickening in the basin amounts a factor of 1.3, whereas in the orogen reaches 1.2. Mantle thickness increases by a factor of 1.7 in the

basin favoured by thermal relaxation, while in the orogen and in the foreland it increases only by a factor of 1.1. Mantle cooling under the basin overcomes tectonic crustal thickening, yielding ~150-m-deeper bathymetry after 25 Myr.

Fig. 5 shows the differences through time in elevation, crustal thickness and lithospheric mantle thickness between the maximum and minimum values for different convergence velocities. Crustal thickening in the orogen is partially compensated by gravitational spreading, which is proportional to topographic gradients. For this reason, considering a fixed amount of shortening (grey dots), lower convergence rates result in lower differences in crustal thickness between orogenic and basinal regions. The final stage of each velocity convergence, after 150 km of shortening, has been aligned (Fig. 5b, thick grey line). The resulting

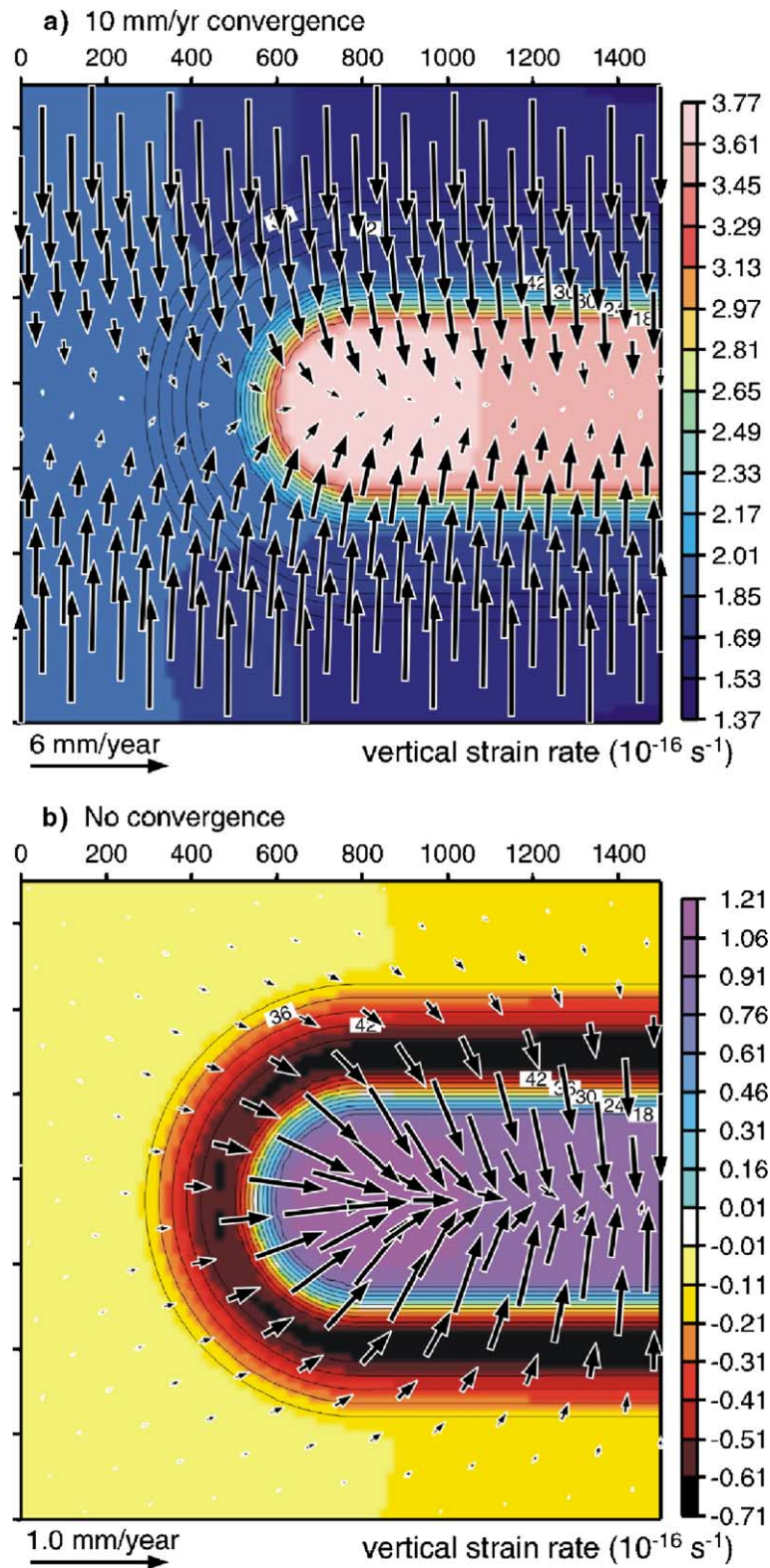


Fig. 3. Initial velocity field (arrows) and vertical strain rate (colours, positive values for thickening and negative for thinning) calculated for the setup shown in Fig. 2. Contours indicate crustal thickness in km. a) Applying a convergence rate of 10 mm/yr (5 mm/yr at the northern and southern boundaries); b) null convergence velocity. Note the different scale of velocity arrows.

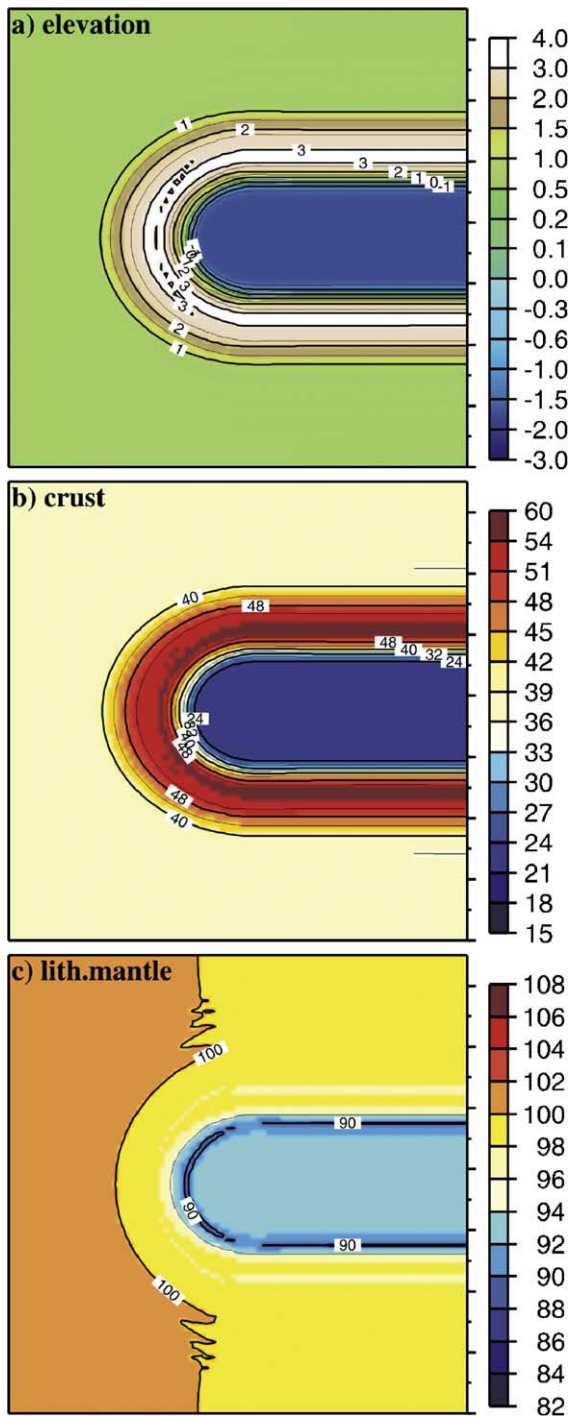


Fig. 4. Elevation (a), crustal thickness (b) and lithospheric mantle thickness (c) attained by Model 1 (reference model) after 25 Myr of 10 mm/yr of convergence rate. Dimensions of model domain: 1500×1500 km.

line presents the same slope as the curve of the model without convergence velocity, and it corresponds to the gravitational spreading of the orogen towards the basin.

However, elevation is also influenced by the lithosphere thermal evolution and hence, the resulting lithospheric structure depends on the convergence velocity, even for equal shortening values. From Fig. 5c, we see how the lithospheric mantle evolution is affected principally by the thermal relaxation, independently from the convergence velocity. Initially the lateral variations of the lithospheric mantle are decreasing due to the quick thermal relaxation compare to the crustal thickening under the basin. Later on (>35 My), the lithospheric mantle thickness is getting thicker under the basin than on the rest of the domain.

4. Effects of lithospheric mantle thickness variations (Model 2)

Model 2 is designed to compare our model to those which do not consider the body forces related to lateral variations of the depth of the lithosphere–asthenosphere boundary (e.g., England and McKenzie, 1983; Sobouti and Arkani-Hamed, 1996; Neil and Houseman, 1997; Marotta et al., 2001). To that purpose, in Model 2 we consider that the base of the lithosphere–asthenosphere boundary is 120 km everywhere, disregarding the temperature reached at this depth, and the mantle lithosphere density is equal to the asthenosphere density. Therefore, Model 2 dismisses the effect of the density contrast between the mantle lithosphere and the asthenosphere in calculating the gravitational potential energy for Eq. (4), and the elevation from local isostasy. The initial crustal thickness is defined identical to Model 1. Because Model 2 does not account for the lithospheric mantle, the initial topography is not the same as in Model 1, in this case varies from -0.41 km (under sea level) in the basin to 3.5 km in the thickened area and 1.6 m in the foreland.

As shown in the previous section, the effective viscosity is highly depending on the ductile stress envelope and hence on the mantle temperature distribution at each lithospheric column. To avoid effects due to the variations on the viscosity pattern, we have assumed the same initial temperature distribution and we have calculated the temperature changes using the same expression from the reference model. Therefore, the differences between Models 1 and 2 would be only due to the lateral variation of the gravitational potential energy.

On Fig. 6, we compare the resulting vertical strain rate, elevation and moho depth between Models 1 and 2 for three different stages (0, 15 and 30 My). The upper panel shows that the vertical strain rate over the orogen for Model 2 is higher than for Model 1, whereas over

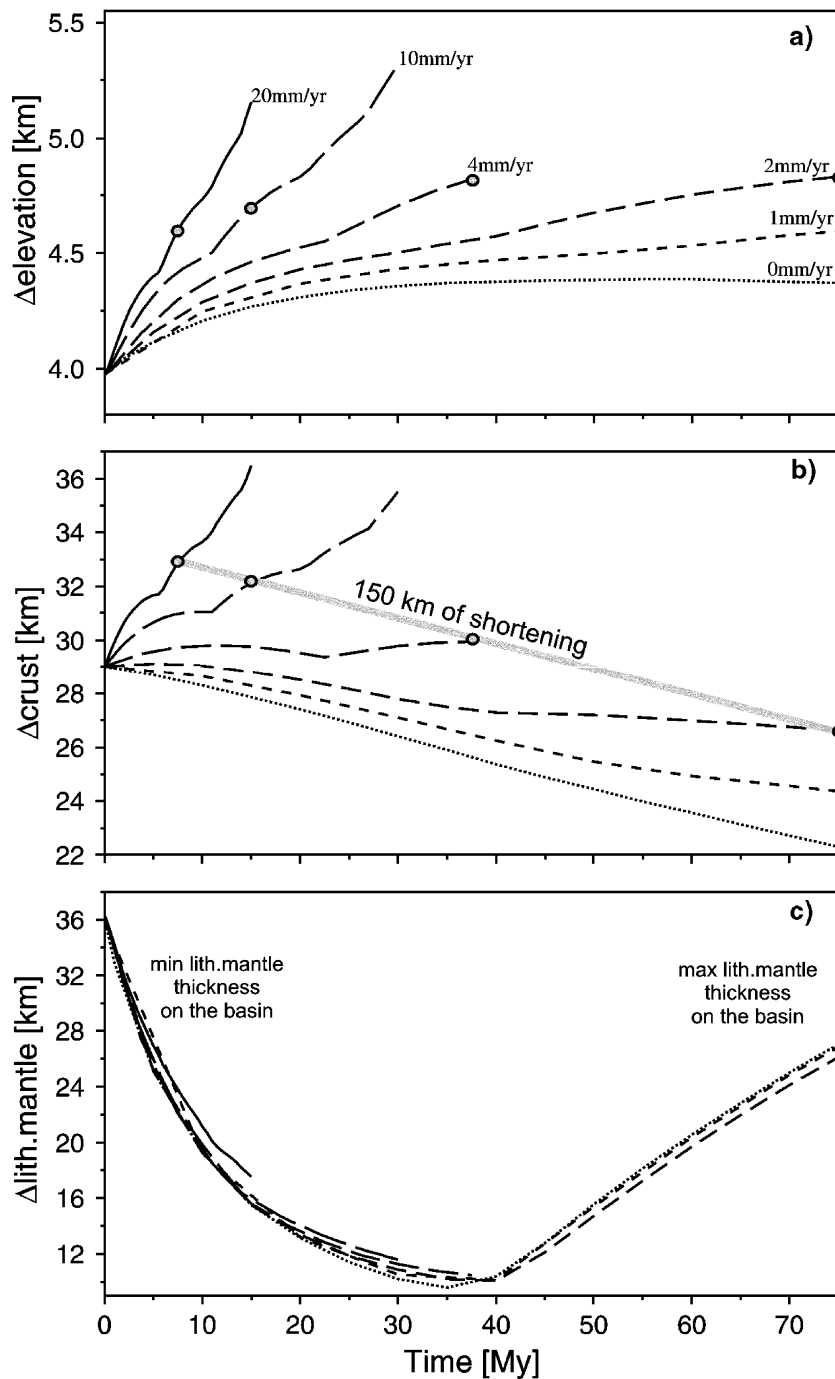


Fig. 5. Effect of convergence velocity on the difference between maximum and minimum elevation (a), crustal thickness (b), and lithospheric mantle thickness (c). Grey dots mark the duration of convergence such that the total amount of shortening is 150 km. The thick grey band in b) shows the effect of the gravitational spreading.

the basin it is the opposite, resulting with a smoother vertical strain rate on Model 2. This is a result from the lateral changes of the gravitational potential energy, which variations are greater in Model 1 than in Model 2. The difference of the gravitational potential

energy between the basin and the orogen is 58% higher in Model 1 than in Model 2. The shallow lithosphere–asthenosphere boundary beneath the basin and the lithospheric root under the orogen helps the mountain belt to collapse gravitationally. In consequence, Model 2

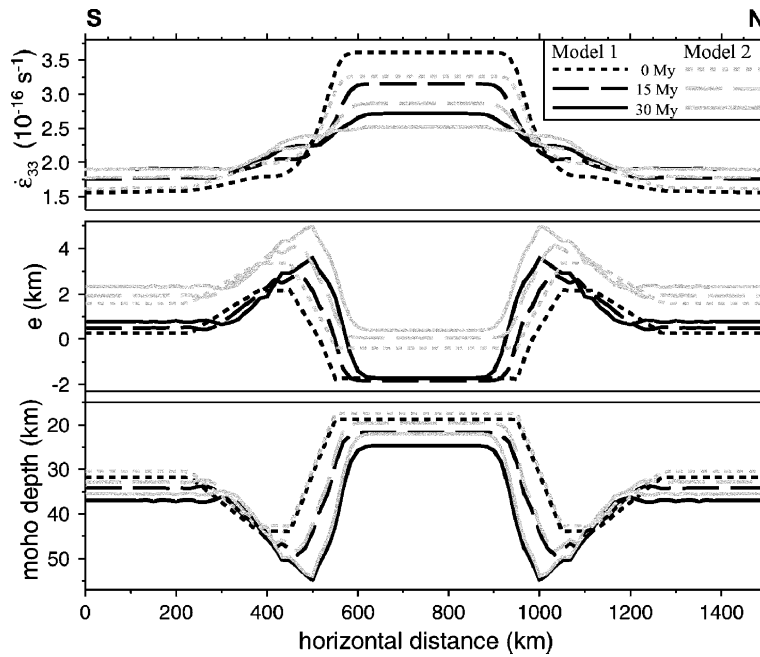


Fig. 6. S–N profiles (section located in Fig. 2a) of Model 1 (black lines) and Model 2 (grey lines) at 0, 15 and 30 My: vertical strain rate ($\dot{\epsilon}_{33}$), elevation (e) and mocho depth.

results, after 30 My, in a near 1 km thicker crust on the orogen and 0.6 km thinner of the basin. The basin is shallowing through time due to the increase in crustal thickness at the expenses of the lithospheric mantle provided that the depth of the base of the lithosphere remains constant. The same reasoning explains the progressive higher topography in the orogenic region.

5. Effects of surface mass redistribution (Model 3)

Model 3 accounts for surface transport of rocks from orogen to the surrounding areas. To implement this process, we adopt a diffusive transport approach in two dimensions according to which surface rock flow \vec{F} is proportional to the local topographic gradient:

$$\vec{F} = -K_d \vec{\nabla} e = -K_d \left(\frac{\partial e}{\partial x}, \frac{\partial e}{\partial y} \right) \quad (8)$$

where K_d is the diffusive coefficient of transport and e is the elevation. Conservation of mass during transport implies that the rate of erosion/sedimentation de/dt is equal to the divergence of \vec{F} :

$$\frac{de}{dt} = -\vec{\nabla} \cdot \vec{F} = K_d \vec{\nabla} \cdot (\vec{\nabla} e) = K_d \left(\frac{\partial^2 e}{\partial x^2} + \frac{\partial^2 e}{\partial y^2} \right) \quad (9)$$

where de/dt is positive for sedimentation and negative for denudation. Sediment deposits are added to a sep-

arate sedimentary body in the code, whereas erosion is subtracted from the uppermost layer (crust or sediment). The sedimentary unit is deformed with the same velocity field as the crust and mantle lithosphere (Eqs. (4) and (5)). Although this approach overlooks the diversity of processes involved in erosion, transport and sedimentation (e.g., landsliding, river incision, etc), it is successful in reducing large-scale elevation differences through time by smoothing the topography, eroding local topographic maxima and filling with sediments local topographic minima. The simplicity of this approach allows for an easy interpretation of the interplay between surface- and lithosphere-scale processes. Previous modelling studies interested in this process interplay have used K_d values of 10^2 – 10^4 m²/yr (e.g., [Flemings and Jordan, 1989](#); [Avouac and Burov, 1996](#)) to simulate the long-term, large-scale surface transport.

Fig. 7 shows the results after 25 My of 10 mm/yr of convergence assuming a diffusive coefficient $K_d=2000$ m²/yr. All other parameters are the same as used in Model 1. Erosion is localised in the elevated areas of the orogen, where up to 10 km of rock are removed, whereas sediments are accumulated in the surrounding areas, particularly in the central basin (Fig. 7b). While sediment thickness reaches values of up to 2 km in the external foreland, the inner basin accumulates more than 7 km, mostly in connection with the deeper initial bathymetry and the fact that it is surrounded by elevated

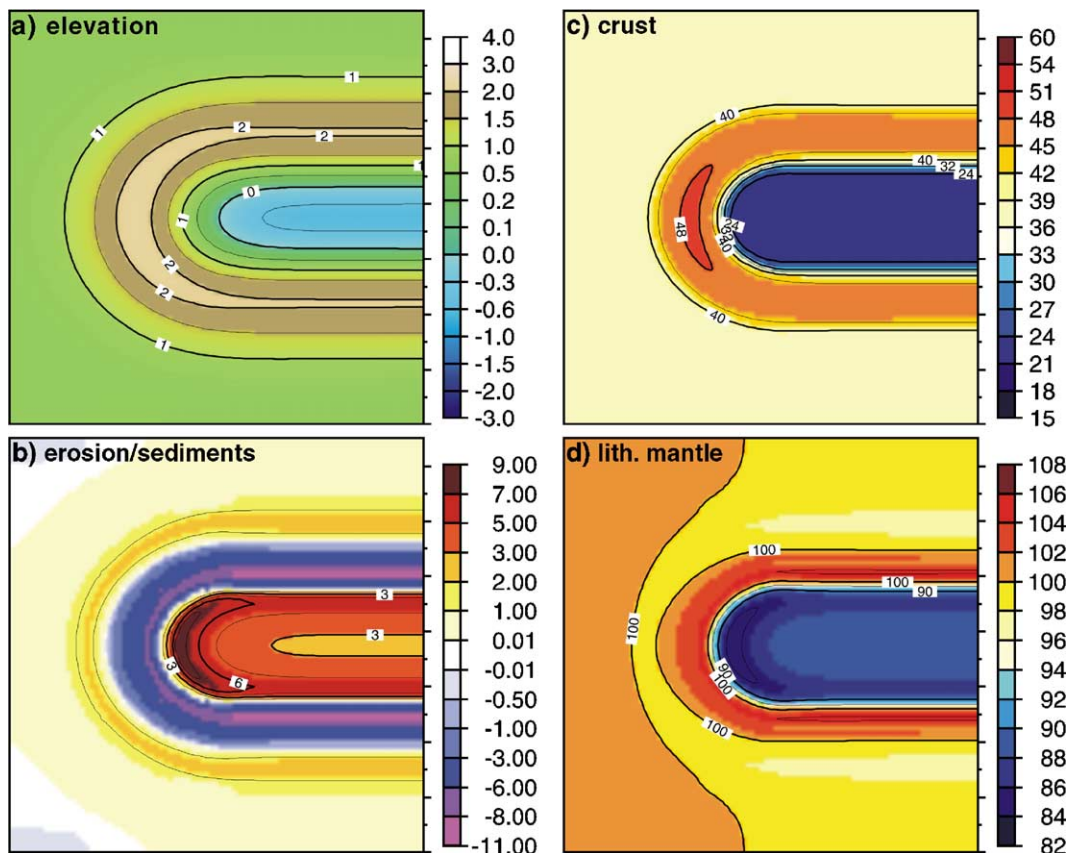


Fig. 7. Results for Model 3 (incorporating erosion and sedimentation) after 25 Myr of 10 mm/yr of convergence rate: a) elevation; b) eroded (negative values) and deposited (positive) thickness; c) crustal thickness (sediments excluded); and d) lithospheric mantle thickness. Dimensions of model domain: 1500×1500 km.

areas. The topography and crustal thickness at this stage (Fig. 7a and c) reflect the effects of surface transport in smoother spatial distributions with less extreme maximum and minimum values (compare to Fig. 4).

A striking result is the prediction that surface transport significantly affects lithospheric mantle thickness thus evidencing the interaction between deep and surface processes. Fig. 7d shows that Model 3 retains a maximum in lithospheric mantle thickness under the orogen, and enhances the minimum values in the basin respect to the reference model (Model 1, Fig. 4c). This is the result of the reduction of crustal thickness of the orogen and the accumulation of sediments (with lower density and thermal conductivity) in the surrounding areas. Therefore, while surface transport reduces lateral contrasts in topography and crustal thickness, it helps to maintain more abrupt thickness variations in the lithospheric mantle. This idea is more conspicuously reflected in Fig. 8, where the differences between the maximum and minimum values of elevation, crustal thickness and lithospheric mantle thickness are repre-

sented against time. Tectonic compression enhances the initial contrasts in crustal thickness and topography and increases through time the effects of gravitational spreading. Surface transport opposes this tendency by smoothing the topographic contrasts. In Model 3, moderate to high erosion rates ($K_d > 700 \text{ m}^2/\text{yr}$) result in a reduction in topographic and crustal thickness contrasts after few million years. Surface transport tends to flatten the top and bottom of the crust, thus reducing gravitational forces and slowing down the gravitational collapse of the orogen, and resulting in a slower reduction of the thickness contrasts of the lithospheric mantle, as seen in Fig. 8c.

Surface transport also influences on the mode of deformation through its effect on the thermal field. Thermal blanketing produced by the low thermal conductivity of sediments favours a slower lithospheric heating. Similarly, erosion at the orogen reduces crustal thickness and decreases the mean temperature of the lithosphere, increasing its strength and delaying its gravitational collapse.

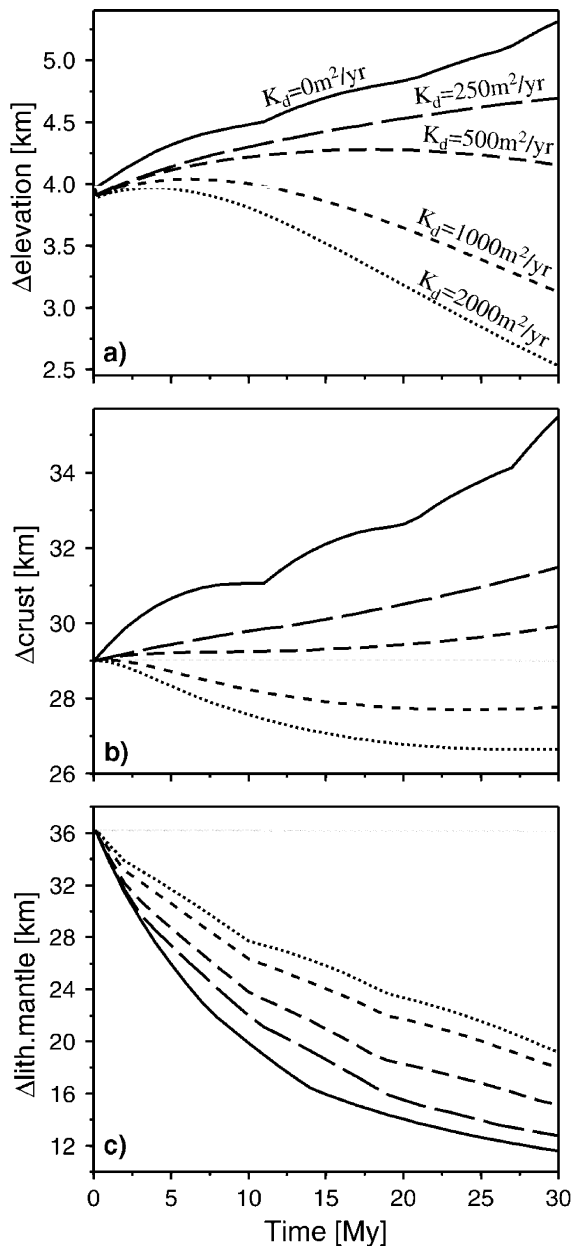


Fig. 8. Effect of diffusive surface transport on the difference between maximum and minimum elevation (a), crustal thickness (b), and lithospheric mantle thickness (c). Each curve corresponds to a different value of diffusive coefficient K_d , indicated in m^2/yr , and the convergence rate is 10 mm/yr.

The combination of these two effects (thermal blanketing and crustal thickness variations), explains the difference between the curves in Fig. 8c. To evaluate the relative importance of these two effects, we run a model identical to Model 3 but using a sediment thermal conductivity equal to that of the crust. The results show that the differences in lithospheric thickness respect to Model 3 were less than 300 m, which indicates

that the role of body forces related to lateral gradients of depth-averaged vertical stress is one order of magnitude higher than that of thermal blanketing.

6. Discussion

Thin-sheet models have been used to study the patterns of crustal/lithospheric thickening and the evolution of stress during continental collision. Extension in overall compressional settings, for example, has been explained as a consequence of lateral variations of gravitational potential energy in a weak crust (average effective viscosity lower than 10^{22} Pa.s; e.g., England and Houseman, 1989; Shen et al., 2001; Liu and Yang, 2003). The model presented here confirms previous results indicating that high potential energy related to elevated topography reduces thickening at elevated zones, eventually producing gravitational spreading of those areas. A soft lithosphere cannot sustain large lateral crust and lithosphere thickness variations, and rock flow from mountain towards the foreland counteracts these lateral variations. At low convergence rates (<3 mm/yr for average lithosphere effective viscosities $\sim 10^{23}$ Pa.s) the gravitational collapse of the mountain will gradually compensate the thickening related to shortening. A wet lithosphere (weak plate, effective viscosity $\leq 10^{22}$ Pa.s) can undergo net extensional collapse also at convergence rates of ~ 10 mm/yr. Therefore, the mode of deformation of the lithosphere is a combination of the lateral gradients of the gravitational potential energy of the lithosphere, the lateral variations of viscosity and the tectonic forces, the two first effects being dominant for moderate-to-low shortening rates (Molnar and Lyon-Caen, 1988). A recent application of this code (Jiménez-Munt et al., in press) shows that the strike-perpendicular extension observed in the western Alps is likely due to lateral variations of gravitational potential energy, while the present rotation of Adria is responsible for the strike-parallel extension and transpression in the eastern Alps.

Our results also emphasize the relevance of buoyancy forces related to the density contrast between lithospheric mantle and asthenosphere. We have seen that an orogen with a prominent lithospheric root located next to a basin with a shallow lithosphere–asthenosphere boundary, may change the mode of lithospheric deformation produced by gravitational collapse of the mountain belt. By considering lateral variations of the depth of the lithosphere–asthenosphere boundary, the presented thin-sheet model is able to predict the evolution of a lithosphere that has lost part of its mantle root by convective removal or delamina-

tion. The effect of the lateral variations of potential energy due to the replacement of lithospheric mantle by lighter asthenosphere results in extension even under high tectonic convergence as it has been proposed by some authors in the Tibetan plateau (England and Houseman, 1989).

Another aspect that has been investigated is the role of radiogenic heat production and its depth distribution. The variations of crustal thickness associated with tectonic collision will change progressively the total radiogenic heat, thus producing a feedback effect on the resulting deformation. This effect depends strongly on the considered depth distribution of radiogenic heat sources such that a higher heat production and deeper distribution implies a higher Moho temperature and a lower effective viscosity. A change in crustal thickness from 46 to 67 km produces an increase in Moho temperature of 25 °C when a constant heat production of $0.6 \mu\text{W m}^{-3}$ is considered, whereas this increase is negligible for an exponential distribution ($H(z) = 2.5 \exp(-z/15) \mu\text{W m}^{-3}$). The deformation field in the north-western Tibetan Plateau has been modelled assuming lithospheric strength variations explained by changes in Moho temperature in the order of 10–30 °C (Neil and Houseman, 1997). Nevertheless, a change of 25 °C in Moho temperature produces a variation on the effective viscosity of around 16%, which indicates that the depth distribution of radiogenic heat sources plays an important role on lithospheric deformation. Moreover, Sandiford et al. (2003) showed that the long-term thermal response to rifting is particularly sensitive to the distribution of heat sources in the crust, changing the lithospheric strength and controlling the localisation of rifting reactivation and basin formation. Therefore, these variations on the Moho temperature induce variations on the effective viscosity of the lithosphere and produce a feedback effect on the resulting deformation. Since experimental studies show that radioactive isotopes are mostly concentrated in silica-rich rocks (e.g., Wollenberg and Smith, 1987), thin-sheet deformation models should incorporate some kind of radiogenic attenuation with depth (e.g., Lachenbruch, 1970).

Cross-sectional analogue and numerical modelling studies have shown that the length-scale of accommodation of shortening in the upper crust (i.e., the propagation of deformation towards the foreland) and the mode of deformation itself are dependent on the spatial distribution of erosion in the uplifted regions (e.g., Jamieson and Beaumont, 1988; Jamieson and Beaumont, 1989; Willet, 1999; Willett and Brandon, 2002; Persson and Sokoutis, 2002). Thin-sheet models have

systematically neglected the effects of surface transport, thus overestimating lateral gravitational forces. The differences between our reference model (Model 1) and that incorporating surface transport (Model 3) show (Fig. 9) that the reduction of crustal thickness and Moho temperature due to erosion results in a significant increase of the effective viscosity of the plate in the orogen (Fig. 9a). Similarly, the accumulation of sediment results not only in an increased pressure in the lithosphere, but also in thermal blanketing and heating up of the plate, reducing its effective viscosity. By changing viscosity, surface transport also shifts the location of thickening (Fig. 9b), increasing it under the sedimentary basins and decreasing it at eroded areas (Fig. 9c).

Thin sheet models do not consider flexure of the lithosphere, failing to account for the subsidence of foreland basins developing at each side of the orogen and, therefore, underestimating sediment accumulation. Surface mass transport affects significantly on the large-scale lithospheric deformation predicted by thin-sheet models (Fig. 9d, e and f). In other words, erosion and sedimentation, rather than acting just as passive processes responding to topographic changes, play an active role in controlling lateral variations of the effective viscosity of the lithosphere and hence of the mode of lithospheric deformation. In our model, erosion modifies the pattern of lithospheric deformation in three ways: 1) by changing lateral depth-averaged vertical stress and gravitational forces in the plate; 2) by changing the thickness and strength of the crust; and 3) by modifying the thermal field at lithospheric scale. These effects would be maximized in settings with high variations of topography favouring sediment accumulation, as well as in places with high surface transport rates. After 30 My of 10 mm/yr of convergence, the lateral variations of the gravitational potential energy between the basin and the orogen is about 50% lower when assuming erosion/sedimentation (Model 3) than without considering surface processes (Model 1). Moreover, sedimentation at 0.4 km/My for 25 My increase the Moho temperature 135°C, reducing the strength of the lithosphere about 50%. Inversely, erosion at 0.4 km/My for 25 My decreases the mean lithospheric temperature, reducing the Moho temperature about 100°C and increasing nearly 60% the strength of the lithosphere. The control on the locus of deformation in central Australia has been attributed to the changes in Moho temperature due to the sediment accumulation (Sandiford and Hand, 1998). Previous thin sheet models have incorporated stiff and weak zones attributed to inherited structures and thermal perturbations, but our

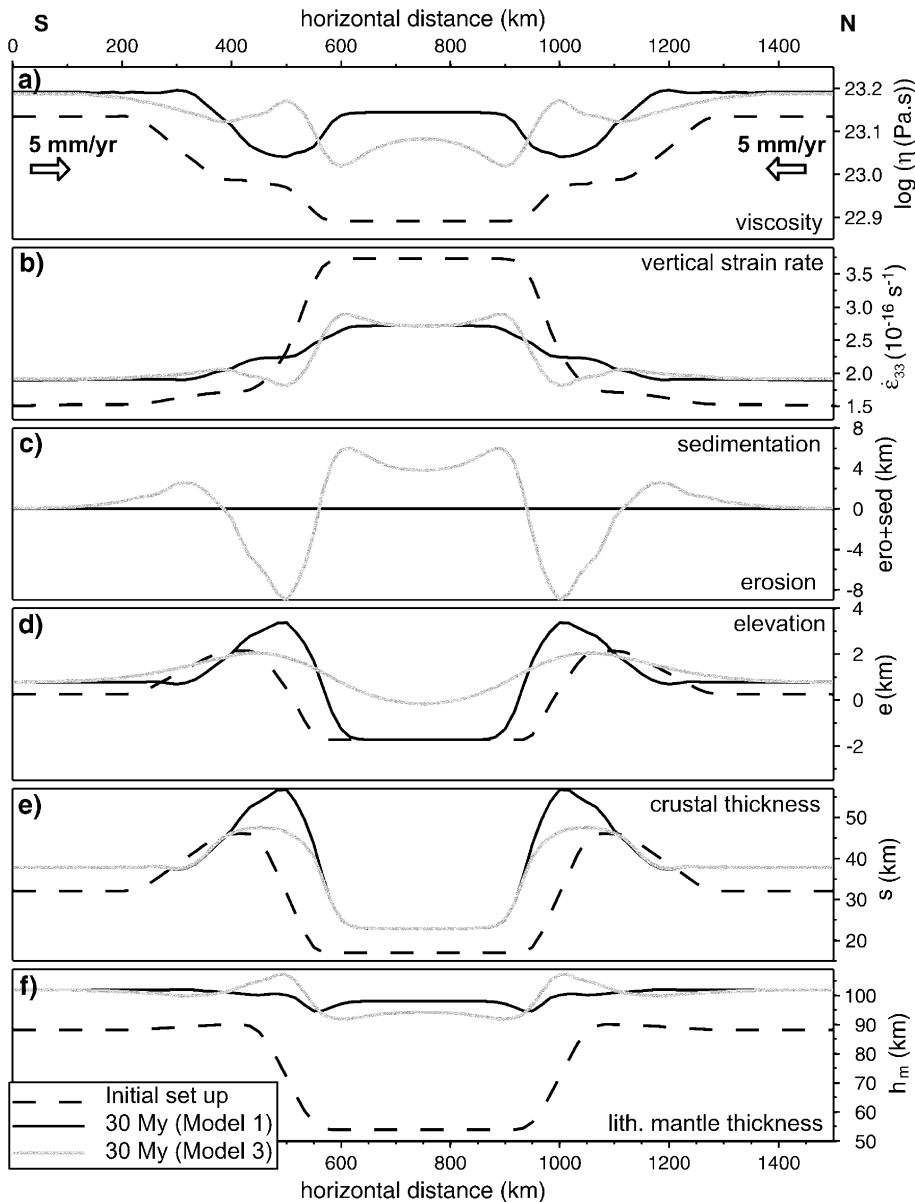


Fig. 9. S–N profiles (section located in Fig. 2a) of the initial set up (black-dashed lines), and after 30 My of 10 mm/yr of convergence rate for Model 1 (without erosion, black lines) and Model 3 (with erosion/sedimentation, grey lines): a) effective viscosity; b) vertical strain rate; c) accumulated erosion (negative values) and sedimentation (positive); d) elevation; e) crustal thickness; f) lithospheric mantle thickness.

results show that lateral changes in crustal/lithospheric strength can be also related to surface mass transport. This result complements the effects of erosion on crustal deformation obtained from cross-section crustal models (Beaumont et al., 1992; Avouac and Burov, 1996; Willet, 1999; Persson and Sokoutis, 2002), and suggests that along-strike variations of topography and sediment transport can induce significant changes on the developing crustal/lithospheric deformation. Effects of the spatial organisation of fluvial networks on crustal deformation (described by Persson et al. (2004)

based on analogue modelling) indicate that future 3D deformation models should be coupled with more detailed surface transport processes.

Acknowledgements

We thank the valuable comments by Greg Houseman, Eric L. Geist, Jean Braun, and an anonymous reviewer. This work is supported by the University College London, the Netherlands Research Centre for Integrated Solid Earth Science (ISES) and the Span-

ish Ministry research projects BTE2002-02462 and REN2001-3868-C03-02/MAR. The authors also benefited from NATO grant EST.CLG.978922.

References

- Avouac, J.P., Burov, E.B., 1996. Erosion as a driving mechanism of intracontinental mountain growth. *J. Geophys. Res.* 101, 17747–17769.
- Beaumont, C., Fullsack, P., Hamilton, J., 1992. Erosional control of active compressional orogens. In: McClay, K.R. (Ed.), *Thrust Tectonics*. Chapman & Hall, London, pp. 1–18.
- Beaumont, C., Kooi, H., Willet, S., 2000. Coupled tectonic–surface process models with applications to rifted margins and collisional orogens. In: Summerfield, M.A. (Ed.), *Geomorphology and Global Tectonics*, pp. 29–55.
- Bird, P., 1988. Formation of the rocky mountains, western United States: a continuum computer model. *Science* 239, 1501–1507.
- Bird, P., 1989. New finite element techniques for modeling deformation histories of continents with stratified temperature-dependent rheology. *J. Geophys. Res.* 94, 3967–3990.
- Braun, J., Shaw, R., 2001. A thin plate model of Paleozoic deformation of the Australian lithosphere: implications for understanding the dynamics of intracratonic deformation. *Geol. Soc. London, Spec. Publ.* 184, 165–193.
- Cloetingh, S.A.P.L., Burov, E., Matenco, L., Toussaint, G., Bertotti, G., Andriessen, P.A.M., Wortel, M.J.R., Spakman, W., 2004. Thermo-mechanical controls on the mode of continental collision in the SE Carpathians (Romania). *Earth Planet. Sci. Lett.* 218, 57–76.
- Cobbold, P.R., Davy, P., Gapais, D., Rossello, E.A., Sadybakasov, E., Thomas, J.C., Tondji Bijo, J.J., de Urreiztieta, M., 1993. Sedimentary basins and crustal thickening. *Sediment. Geol.* 86, 77–89.
- Ellis, S., Fullsack, P., Beaumont, C., 1995. Oblique convergence of the crust driven by basal forcing: implications for length-scales of deformation and strain partitioning in orogens. *Geophys. J. Int.* 120, 24–44.
- England, P., Houseman, G., 1985. Role of lithospheric strength heterogeneities in the tectonics of Tibet and neighbouring regions. *Nature* 315, 297–301.
- England, P., Houseman, G., 1989. Extension during continental convergence, with application to the Tibetan Plateau. *J. Geophys. Res.* 94, 17561–17579.
- England, P., McKenzie, D.P., 1983. Correction to: a thin viscous sheet model for continental deformation. *Geophys. J. R. Astron. Soc.* 73, 523–532.
- Fernández, M., Ranalli, G., 1997. The role of rheology in extensional basin formation modelling. *Tectonophysics* 282, 129–145.
- Flemings, P.B., Jordan, T.E., 1989. A synthetic stratigraphic model of foreland basins development. *J. Geophys. Res.* 94, 3851–3866.
- García-Castellanos, D., Fernández, M., Torne, M., 2002. Modelling the evolution of the Guadalquivir foreland basin (south Spain). *Tectonics* 21. doi:10.1029/2001TC001339.
- Goetze, C., Evans, B., 1979. Stress and temperature in the bending lithosphere as constrained by experimental rock mechanics. *Geophys. J. R. Astron. Soc.* 59, 463–478.
- Jamieson, R.A., Beaumont, C., 1988. Orogeny and metamorphism: a model for deformation and P – T – t paths with applications to the central and southern Appalachians. *Tectonics* 7, 417–445.
- Jamieson, R.A., Beaumont, C., 1989. Deformation and metamorphism in convergent orogens: a model for uplift and exhumation of metamorphic terrains. In: Daly, J.S., Cliff, R.A., Yardly, B.W.D. (Eds.), *Evolution of Metamorphic Belts*, *Geol. Soc. Spec. Publ.*, vol. 43, pp. 117–129.
- Jiménez-Munt, I., Fernández, M., Torne, M., Bird, P., 2001. The transition from linear to diffuse plate boundary in the Azores–Gibraltar region: results from a thin-sheet model. *Earth Planet. Sci. Lett.* 192, 175–189.
- Jiménez-Munt, I., Sabadini, R., Gardi, A., Bianco, G., 2003. Active deformation in the Mediterranean from Gibraltar to Anatolia inferred from numerical modeling and geodetic and seismological data. *J. Geophys. Res.* 108. doi:10.1029/2001JB001544.
- Jiménez-Munt, I., García-Castellanos, D., Negro, A.M., Platt, J.P., in press. Gravitational and tectonic forces controlling the post-collisional deformation and present-day stress of the Alps. Constraints from numerical modelling. *Tectonics*.
- Lachenbruch, A., 1970. Crustal temperature and heat production: implications of the linear heat flow relation. *J. Geophys. Res.* 75, 3291–3300.
- Liu, M., Yang, Y., 2003. Extensional collapse of the Tibetan Plateau: results of three-dimensional finite element modelling. *J. Geophys. Res.* 108. doi:10.1029/2002JB002248.
- Lynch, H.D., Morgan, P., 1987. The tensile strength of the lithosphere and the localization of extension. In: Coward, H.D., Dewey, J.F., Hancock, P.L. (Eds.), *Continental Extension Tectonics*, *Geol. Soc. Spec. Publ.*, vol. 28, pp. 53–65.
- Marotta, A.M., Bayer, U., Scheck, M., Thybo, H., 2001. The stress field below the NE German Basin: effects induced by the Alpine collision. *Geophys. J. Int.* 144, F8–F12.
- Molnar, P., Tapponnier, P., 1981. A possible dependence of tectonic strength on the age of the crust in Asia. *Earth Planet. Sci. Lett.* 52, 107–114.
- Molnar, P., Lyon-Caen, H., 1988. Some simple physical aspects of the support, structure, and evolution of the mountain belts. *Geol. Soc. Am.* 218, 179–207.
- Morgan, P., Sawka, W.N., Furlong, K.P., 1987. Background and implications of the linear heat flow–heat production relationship. *Geophys. Res. Lett.* 14, 248–251.
- Mugnier, J.L., Baby, G., Colletta, B., Vinoue, P., Bale, P., Leturmy, P., 1997. Thrust geometry controlled by erosion and sedimentation: a view from analogue models. *Geology* 25, 427–430.
- Neil, E., Houseman, G., 1997. Geodynamics of the Tarim Basin and the Tian Shan in central Asia. *Tectonics* 16, 571–584.
- Persson, K.S., Sokoutis, D., 2002. Analogue models of orogenic wedges controlled by erosion. *Tectonophysics* 356, 323–336.
- Persson, K.S., García-Castellanos, D., Sokoutis, D., 2004. River transport effects on compressional belts: first results from an integrated analogue–numerical model. *J. Geophys. Res.* 109. doi:10.1029/2002JB002274.
- Pollack, H.N., Chapman, D.S., 1977. On the regional variation of heat flow, geotherms and lithospheric thickness. *Tectonophysics* 38, 279–296.
- Ruddiman, W.F., 1997. *Tectonic Uplift and Climate Change*. Plenum, New York, pp. 535.
- Sandiford, M., Hand, M., 1998. Controls on the locus of intraplate deformation in central Australia. *Earth Planet. Sci. Lett.* 162, 97–110.

- Sandiford, M., Frederiksen, S., Braun, J., 2003. The long-term thermal consequences of rifting: implications for basin reactivation. *Basin Res.* 15, 23–43.
- Shen, F., Royden, L.H., Burchfield, B.C., 2001. Large-scale crustal deformation for the Tibetan Plateau. *J. Geophys. Res.* 106, 6793–6816.
- Sobouti, F., Arkani-Hamed, J., 1996. Numerical modelling of the deformation of the Iranian plateau. *Geophys. J. Int.* 126, 805–818.
- Sonder, L.J., England, P., 1986. Vertical averages of rheology of the continental lithosphere: relation to thin sheet parameters. *Earth Planet. Sci. Lett.* 77, 81–90.
- Sonder, L.J., England, P., 1989. Effects of a temperature-dependent rheology on large-scale continental extension. *J. Geophys. Res.* 94, 7603–7619.
- Tommasi, A., Vauchez, A., Daudré, B., 1995. Initiation and propagation of shear zones in a heterogeneous continental lithosphere. *J. Geophys. Res.* 100, 22083–22101.
- Torne, M., Fernandez, M., Comas, M.C., Soto, J.I., 2000. Lithospheric structure beneath the Alboran basin: results from 3D gravity modelling and tectonic relevance. *J. Geophys. Res.* 105, 3209–3228.
- Vilotte, J.P., Daignières, M., Zienkiewicz, O., 1982. Numerical modelling of intraplate deformation: simple mechanical models of continental collision. *J. Geophys. Res.* 87, 10709–10728.
- Vilotte, J.P., Madariaga, R., Daignières, M., Zienkiewicz, O., 1986. Numerical study of continental collision: influence of buoyancy forces and an initial stiff inclusion. *Geophys. J. R. Astron. Soc.* 84, 279–310.
- Willet, S.D., 1999. Orogeny and orography: the effects of erosion on the structure of mountain belts. *J. Geophys. Res.* 104, 28957–28981.
- Willet, S.D., Brandon, M.T., 2002. On steady states in mountain belts. *Geology* 30, 175–178.
- Wollenberg, H.A., Smith, A.R., 1987. Radiogenic heat production of crustal rocks: an assessment based on geochemical data. *Geophys. Res. Lett.* 14, 295–298.